

# Characterization of Hammamatsu Multianode Photo Multiplier Tubes H8500 and H12700

P. Degtiarenko<sup>a</sup>, A. Kim<sup>b\*</sup>, V. Kubrovsky<sup>a</sup>, A. Smith<sup>c</sup>

<sup>a</sup>*Jefferson Lab, Newport News, Virginia, USA*

<sup>b</sup>*University of Connecticut, Storrs, CT 0626, USA*

<sup>c</sup>*Duke University, Durham, NC 2770, USA*

---

## Abstract

Characterization of Hammamatsu Multianode Photo Multiplier Tubes H8500 and H12700.

**Keywords:** Ring Imaging Cherenkov detector, Multianode Photo Multiplier tubes H8500 and H12700, Photon detector, Photomultiplier, Photoelectron, Signal amplitude spectra, Photon detection efficiency

---

---

\*Corresponding author Tel: +1 757 269 6356  
Email address: kenjo@jlab.org (A. Kim )

## 1. Introduction

As part of the ongoing study of the structure of nucleons [1] in Hall B at the Thomas Jefferson National Accelerator Facility (JLab) the CEBAF Large Acceptance Spectrometer (CLAS12) [2] aims to accurately identify the secondary particles of high energy reactions, assist in probing the strangeness frontier, and aid in characterizing transverse momentum distribution (TMD) and generalized parton distribution (GPD) functions. Indispensable to this task is the ability to identify kaons, pions, and protons. With the CLAS12 spectrometer providing accurate momentum measurements the Ring imagine Cherenkov detector (RICH) [3, 4, 5, 6] provides tandem Cherenkov light-cone radius measurements which yield the velocities of near light-speed particles, thus facilitating mass-dependent particle identification.

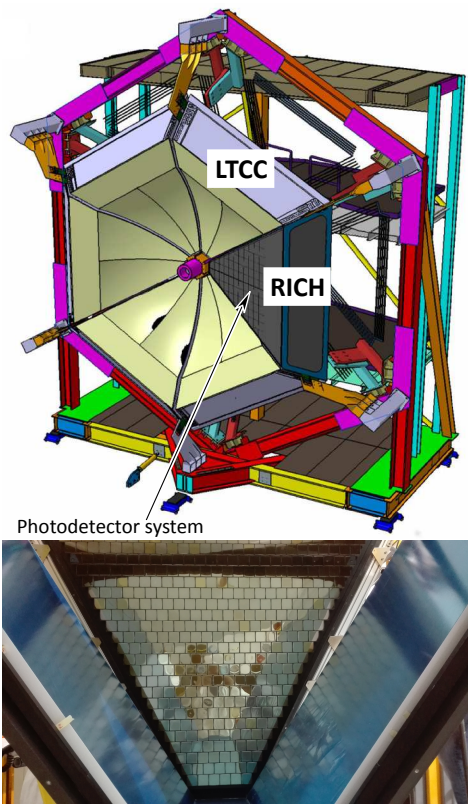


Figure 1: Top: CLAS12 detector with RICH detector covering one out of six sectors. Bottom: the photo-matrix of multianode photomultipliers and mirror system.

The photon detector wall ( $\sim 1m^2$ ) is a crucial component of the RICH detector (see Fig. 1). It is relatively large and should be comprised of many photon detection devices such as photomultiplier tubes. Due to the imaging aspect of the RICH they must provide a spatial resolution of less than 1 cm. Since multiple photon detectors are tiled into large arrays, they should have large active area with minimal dead-space. The photon detectors must also efficiently detect single photon level signals and should be sensitive to the visible light due to the aerogel radiator material. Multi Anode PhotoMultiplier Tubes (MAPMTs) are perfect candidates for the CLAS12 RICH de-

tector. They are the flat-panel Hamamatsu MAPMTs offering an adequate compromise between detector performance and cost. Each MAPMT comprises an 8 by 8 array of pixels, each with dimension of 6 by 6 mm. Furthermore, the device has a very high packing fraction of 89% with a high quantum efficiency in the visible light region. The tubes also have excellent immunity to magnetic fields, because all internal parts are housed in a metal package and the distance between dynode electrodes are very short.

Initially, the Hamamatsu H8500 MAPMT model [7] was chosen as the best option because they provide high quantum efficiency for visible light and sufficient spatial resolution ( $6 \times 6 \text{ mm}^2$ ) at a limited cost. However, recently Hamamatsu has released the new H12700 MAPMT model which shows enhanced single photoelectron (SPE) detection and is otherwise similar to the H8500 MAPMTs in spatial resolution and cost. Consequently we desire to better characterize the new H12700 MAPMTs [8] and choose the best model between these two options for inclusion in the CLAS12 RICH.

## 2. Laser stand for the MAPMT characterization

The large number of the channels in the RICH detector poses challenging problem for the MAPMT testing and calibration. RICH consists of 391 MAPMTs resulting in total number of channels equal to 25024. So in order to test them efficiently within a reasonable timeframe the fully automated test stand was build to evaluate 6 MAPMTs at once, as shown on Fig. 2.

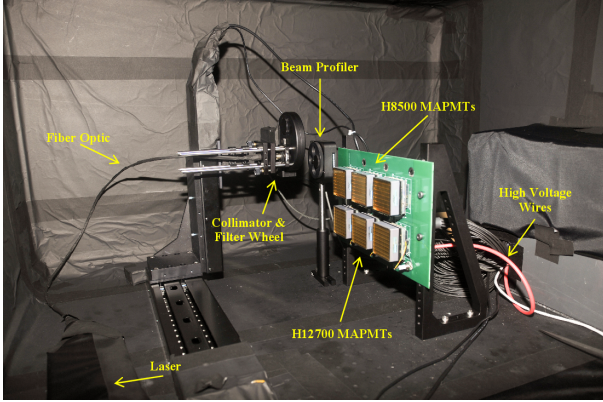


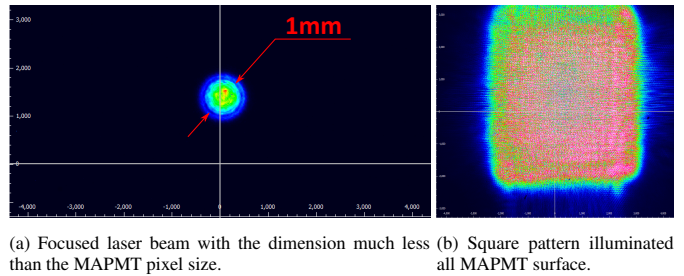
Figure 2: Inner view of the laser stand.

The test stand consists of picosecond diode laser PiL047X with 470 nm wavelength, 2 long travel motorized stands to drive laser fiber in two dimensional space for individual pixel illumination, the motorized wheel with neutral density filter system, 2 adapter boards for MAPMT with JLab designed front-end electronics boards [Contalbrigo:2020]. The laser light is directed through the fiber and attenuated to the single photon level using the neutral density filters to mimic the conditions of the RICH detector. The motors were remotely controlled to move the focused laser beam across (see Fig. 3a) the entire surface of the MAPMT entrance window and illuminate one by one of all its 64 pixels individually. Another option is to illuminate the whole surface of MAPMT photocathode at once using the Engineered Diffuser to produce square pattern with non-Gaussian intensity distribution (see Fig. 3b).

All laser stand equipment is sitting in the black box with non-reflective black material on the optical table. The laser interlock safety box automatically switch off laser, as well as front-end low voltage electronics and MAPMT high voltage to prevent the possible photomultiplier damage or laser light human illumination in case if somebody will try to open the front door of the black box during the measurements.

This configuration brings routine workload to minimum allowing the evaluation of 6 MAPMTs (equivalent to 328 conventional PMTs!) at 4 different high voltages and 6 different light intensities within 6 hours with less than 15 minutes of human intervention needed to load the MAPMTs to the front-end boards.

Before starting the systematic study of the MAPMT responses, a finer two dimensional scan of several pixels was performed in order to verify the uniformity of the response across pixel's surfaces, as shown on Fig. 4. The horizontal and vertical axes denote laser beam position during the scan. Along the both



(a) Focused laser beam with the dimension much less than the MAPMT pixel size.  
(b) Square pattern illuminated all MAPMT surface.

Figure 3: The laser light output options.

directions there are obvious drops in efficiency when the laser strikes the space between the pixels. The drops are relatively narrow so the dead-space is very small as expected from the Hamamatsu specifications. Additionally, a vertical efficiency variation is visible across the pixel in horizontal scan. These inhomogeneities are correlated with the vertical walls separating dynode chains, owing to the constructional features of the MAPMT. The discontinuity in dynode structure is visible on Fig. 4a. The separate response maps for photocathode shows relatively uniform signal without efficiency drops, confirming that the variation arises from the dynode system.

## Front-end electronics

The highly integrated front-end electronics with modular design was developed for a large array of MAPMT H12700 to minimize the impact of the electronics material on the detector downstream the RICH. An architecture of the readout electronics consists of front-end cards with dedicated Application Specific Integrated Circuit (ASIC) configured, controlled and read-out by programmable devices such as Field Programmable Gate Array (FPGA). The ASIC board is based on the MAROC3 integrated circuit whose excellent single photon capabilities both in analog and binary mode have been confirmed. The final design has consists of stacked PCB layers behind each MAPMT sensor (see Fig. 5). The first layer houses the ASIC front end and ancillary components (e.g. external amplifier) and it is directly connected to the anodes array. A second PCB will host the FPGA in charge of configuring, managing and acquiring one or more ASICs and the low voltage and HV bias distribution. The use of the JLab SSP as controller and collector of the front-end data provides a strong synergy with the current JLab upgrade

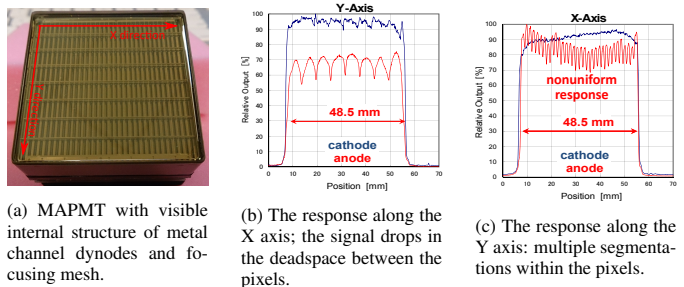


Figure 4: The response uniformity of MAPMT.

activity. Data are transmitted on high speed serial (optical) lines minimizing the wiring and therefore the material budget. With that sandwich architecture the total photon detection surface will be covered by a fixed number of basic units or tiles made up by two or three sensor each. The total spacing for electronics will not exceed 20 cm in depth (including MAPMT and mechanical support). The three-tiles electronics module with and without 3 H12700 MAPMTs installed is shown on Fig. 5.

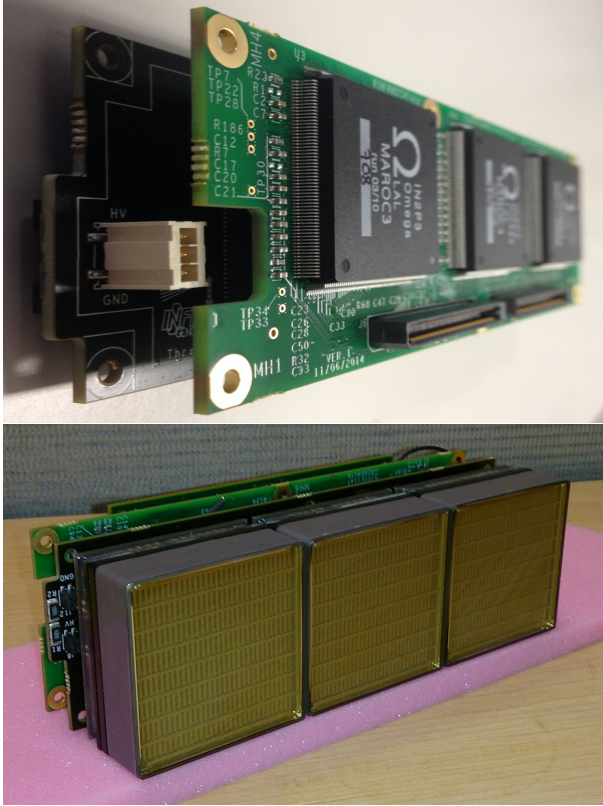


Figure 5: Front-end electronics readout board and mounted MAPMTs.

The MAROC chip consists of 64 independent channels. The single channel has a pre-amplification and configurable 8 bit gain correction stage followed by independent binary and analog lines. The binary line is digital and most suitable for the RICH application. We are planning to analyze the performance of MAROC chip as a function of its threshold and gain. Additionally front-end electronics stability and noise will be tested as well.

## Front-End Electronics for RICH

Due to the high number of active channels in readout subsystem of the RICH detector and available limited space the Multi Anode ReadOut Chips (MAROC) were chosen to construct highly integrated front-end electronics with modular design. The MAROC performances were checked and found suitable for the RICH requirements. Each chip is equipped with single channel adjustable preamplifier, configurable signal shaping, slow shaper capable of charge measurements and binary output with fast shaping and adjustable threshold. The custom

modular design as shown on Fig. ?? consists of sandwich architecture where one board hosts the ASIC chips (2 or 3 per board) and another active board hosts the FPGA to manage and configure the ASICs, the third board is a passive adapter for MAPMT sockets. It satisfies the following requirements:

- 100% efficiency at 1/3 of single photoelectron signal (50 fC)
- time resolution of 1 ns
- short deadtime to sustain the trigger rate of 20 kHz
- latency of 8  $\mu$ s

The conceptual design of the electronics readout boards was finished in the RICH development phase and currently we have several board implementations available at Jefferson Lab and INFN for final tests.

The preliminary measurements with internal onboard charge injector, external charge injector and signal generator were performed to test and calibrate FE electronics. However, the measurements of custom front-end electronics together with installed MAPMTs in the RICH Black Box setup are crucial for understanding their future performance in the RICH detector in CLAS12. RICH MAPMT test setup was modified to house two FE board at once inside the black box as shown on Fig. 6. The focus of the modification was to adapt the test setup in such way that the swap of FE boards would be fast and easy. The PCB guidelines were installed inside the black box to ensure easy mounting and dismounting procedure universal for both 2-MAPMT and 3-MAPMT FE modules. This requirement exists in light of the future measurements that our group is expected to perform on all FE modules for testing purposes. Each FE module is connected to the low voltage power supply to power FPGA and ASIC boards. The communication between FPGA board and PC is performed using TCP/IP protocol via optical fiber network cable. The HV cables, one per each module, supply power for attached MAPMTs. The Data Acquisition program runs on external PC under Linux OS, configures FPGA and MAROC boards and collects the data through the network interface. As before the laser with neutral density filters and light diffuser is installed on moving platform to allow illumination of individual MAPMTs with different light intensities. The current setup allows fast evaluation of FE modules with highly automated procedure which is important because RICH will be utilizing 113 tiles with 3 MAPMTs and 23 tiles with 2 MAPMTs FE modules to house 391 MAPMTs.

The planned measurements will group individual boards with MAPMTs and treat them as a inseparable unit that will go into the final assembly of RICH detector. Every unit will be tested in the black box setup to mimic the conditions of SPE regime expected during the RICH routine operations. The calibration procedures will be developed and evaluated during these test measurements. The gain equalization, individual channel amplification parameters and optimal threshold values will be investigated and resolved. In addition, self-triggering capabilities of FE modules allow careful dark current measurements. The previous measurements and evaluation of MAPMTs with

different readout systems (JLab FADC) will be compared with FE measurements to better understand the MAPMTs and FE performances. The calibration procedures will be developed and evaluated during these test measurements.

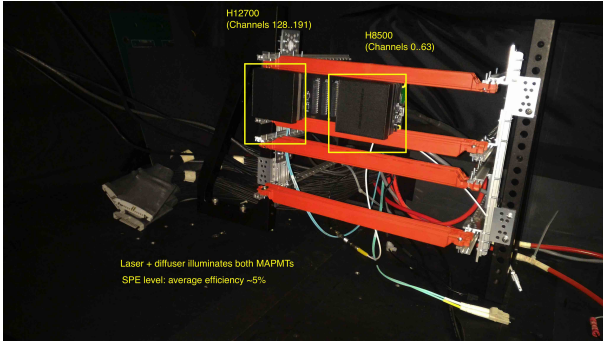


Figure 6: Mount inside RICH Black box is capable to hold two Front-End boards and up to 6 MAPMTs

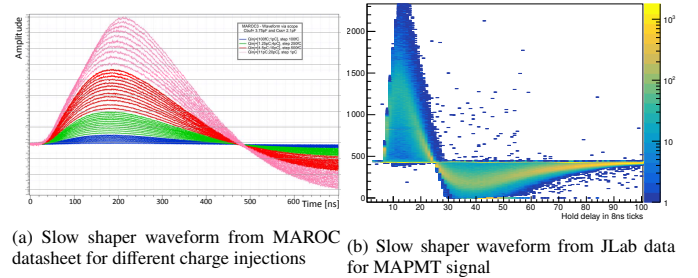
The MAROC chip used to read MAPMT outputs has two main paths to feed the preamplified input current:

- analog line with a slow shaper which allow the injected charge measurements
- binary line with a fast shaper followed by a discriminator with configurable threshold which allows to deliver trigger outputs

Both lines are independent and highly configurable. The slow shaper can not be used during normal operation of RICH detector due to relatively small HOLD latency of 200 ns. It can, however, be used for calibration purposes. On the other hand the digital line with fast shaper is suitable for RICH operation and will be used to detect signals from Cherenkov photons incident on the readout panel.

The preliminary measurements of MAPMTs signal were taken using the FE tile with 3-MAPMTs installed inside the RICH black box. Both lines were evaluated as shown of Fig. 7 and 8. The internal pulse generator was used to trigger laser through its adjustable external trigger input achieving synchronization between light source and MAROC readout. Then the data were collected with both lines collecting data in parallel. Fig. 7a shows the slow shaper waveform for different charge injections from MAROC3 datasheet. On the right Fig. 7b shows the same waveform obtained from the data collected at Jefferson Lab using RICH test setup with laser and MAPMT. In order to reconstruct the waveform of the slow shaper, the hold delays parameters was changed from 1 to 100 and data were collected at different values. This measurements allow us to find the best value of the hold delay for internal ADC conversions which correspond to the signal maximum at around (13 ticks = 104 ns). It ensures the largest precision to the charge measurements. The shape of the analog output waveform is configurable and its gain and peaking speed can be changed.

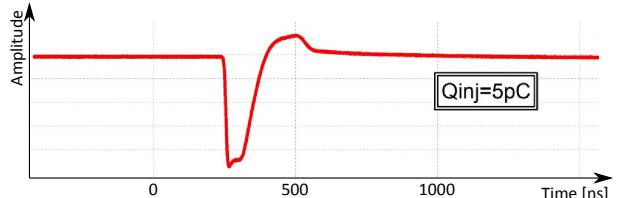
The digital line can be sampled with a predefined clock on an adequate deep external digital pipeline with event information available promptly in parallel making it suitable for



(a) Slow shaper waveform from MAROC

(b) Slow shaper waveform from JLab data for MAPMT signal

Figure 7: Slow shaper response from MAROC



(a) Fast shaper waveform from MAROC datasheet

(b) Measured dependency of "time over threshold" vs threshold

Figure 8: Fast shaper response from MAROC

the RICH application. The binary information comes from the discrimination of the fast shaper lines output. On Fig. 8a the fast shaper waveform is shown for fixed injected charge from MAROC3 datasheet. On the right fig. 8b shows the the dependence of time over threshold versus threshold values. The digital line reports the time when fast shaper waveform crosses the threshold value giving us the leading and trailing edges. To reconstruct fast shaper waveform the measurements with different threshold values were collected and the time of leading and trailing edges were plotted. As expected at higher thresholds the signal crosses the threshold later and has a shorter time over threshold. Also the spread of SPE response from MAPMT gives us preliminary indication of signal's time walk which can be further corrected to improve time resolution. The behaviour at high threshold might not represent the expected performance because the signal reaches saturation and loses its linearity.

Preliminary measurements of MAROC3 and MAPMTs demonstrate good time and charge resolution allowing to further improve our MAPMTs measurements and their understanding. The final production of FE boards is nearly complete and we expect to start receiving FE tiles within the next month.

### Typical fit of single photoelectron spectrum

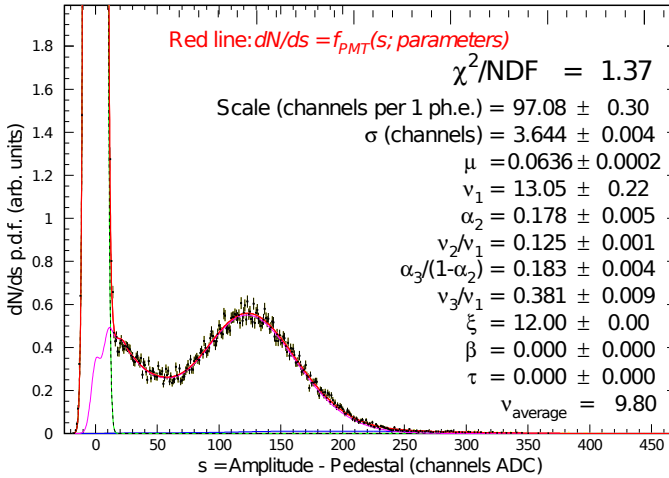


Figure 9: Sample of single photoelectron spectrum from one of the pixels at 1000 V with low intensity laser light source, where integer  $m$  corresponds to the number of photoelectrons created at the first stage of the photodetector (photocathode) by the incident light during one event of radiation, index  $n$  corresponds to the number of electrons generated at the second stage of the photodetector (first dynode).

### 3. Mathematical model for the description of the PMT's response

We started by using a model for signal amplitude distribution based off of Gaussian single photoelectron spectra as discussed in [9] that works reasonably well for H8500, but this model does not satisfactorily treat the spectra seen in the new H12700 MAPMTs from Hamamatsu. Consequently, Pavel Degtarenko [10] has developed a more complicated model using several Poisson components to better fit the MAPMT spectra, especially in the single photoelectron cases. This mathematical model features a realistic description of the MAPMT response where each parameter corresponds to the physical process inside the MAPMT. The SPE spectrum is fitted with a function used to describe the signal amplitude distribution measured by the MAPMT as shown on Fig. 9, The probability of an initial photon to knock out a photoelectron is distributed according to the Poissonian  $P(m; \mu) = \frac{\mu^m e^{-\mu}}{m!}$ . To approximate the performance of the first amplification cascade of the MAPMT the function  $T(n, m; t)$  is introduced in the model as trinomial sum of three Poissonians with different average secondary multiplicities and the corresponding three relative probabilities for every photoelectron to generate secondary electrons. The function  $G(a, n; \sigma)$  corresponds to the realistic DAQ measurement function to introduce the experimental resolution into the resulting model function.

The model is found to describe well the amplitude distributions measured at different levels of radiation with different supply voltages. The parameters provide MAPMT characteristics independently of the test measurement conditions (see Fig. 10): the *scale* parameter is virtually independent on the light radiation level while strongly dependnt on high voltage supply, the exact behavior one would expect from the characteristic of internal dynode system of MAPMT.

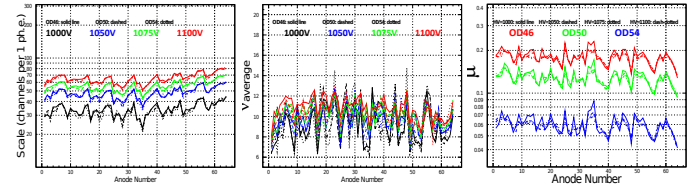


Figure 10: Distributions of fit parameters among the pixels for measurements with 4 different high voltage supplies and 3 different light intensities: the parameter *scale* characterizes the amplification (dynode) system,  $\nu$  - first dynode performance,  $\mu$  relates to the quantum efficiency (photocathode performance).

Currently we have tested 80 H8500 and 260 H12700 (the largest collection of these new MAPMTs in the world). The accumulated data provide an immense knowledge about quantum and collection efficiencies of MAPMTs, their surface uniformity, single photoelectron (SPE) spectrum resolution etc. This parameterized information extracted from the fit of each pixel for every MAPMT is used to describe the detector response in the future simulation.

#### 4. Characterization of MAPMTs

The performance of MAPMTs was evaluated under certain high voltages. The single photoelectron spectrum and the pixel efficiency for H12700 MA-PMTs were tested and analyzed at 1000v, 1050v, 1075v, and 1100v. The measurements performed at the reference supply voltage of 1000 V were compared to the measurements at different HV values in order to study the behavior of the MAPMT response as a function of the supply voltage. As expected, it was found that the H12700 MA-PMTs perform the best in the single photoelectron spectrum efficiency at higher voltages, especially at 1100v. We see a significantly improved separation of the first photoelectron peak from the pedestal at higher voltage supplies (see Fig. 11). When the average deficiencies of the tested MA-PMTs were analyzed, it was found that the average efficiency for 1000v, 1050v, 1075v and 1100v were approximately 4.6%, 4.9%, 5.0%, and 5.2%, respectively. Therefore, the increase in detection efficiency is found to be over 10% at 1100 V in comparison to 1000 V supply. This separation is the crucial point for a single photon counting detectors such as CLAS12 RICH, where the occupancy is at the level of one photon per pixel.

It was also found that as the gain of the MAPMT increased, the efficiency ratio of 1100v to 1000v decreased. The ratio is shown on Fig. 12 as a function of MAPMT gain reported by Hamamatsu. The high voltage supply improves the performance of MAPMT dynode system, decreasing the fraction of the single photoelectron events below the pedestal peak. This indicates that lower gain MAPMTs have a greater difference in the efficiencies at 1100v and 1000v, while higher gain MAPMTs have a smaller difference between the two voltage efficiencies. The improvement for lower gain MAPMTs is more significant than for higher gain MAPMTs, because the high gain MAPMT has good separation of signal from pedestal even at the reference 1000 V. Therefore, the low gain MAPMT benefit greatly from higher supply voltage. The collected data are used to determine what high voltage the MAPMTs should be ran at to acquire the best results when the RICH detector is completed.

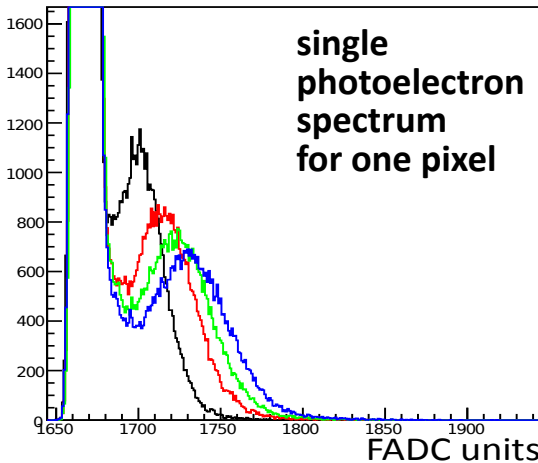


Figure 11: SPE spectra at 1000 (black), 1050 (red), 1075 (green) and 1100 (blue) V.

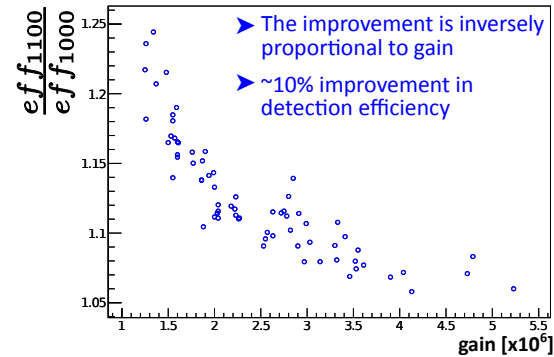


Figure 12: Ratio of MAPMT efficiencies at 1100 and 1000 V as a function of MAPMT gain.

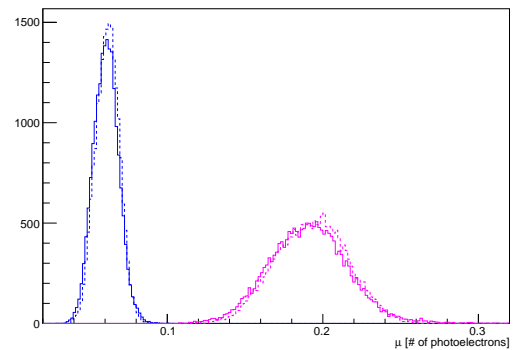


Figure 13: Average number of the photoelectrons emitted from the photocathode for different laser light intensities:  $10^{-5.4}$  - blue and  $10^{-4.6}$  - red. Solid line is for measurements at 1000 V and dashed - at 1100 V

The parameters from Pavel's PMT response function are shown on the Fig. 13 and 14 and correspond to the emission of the photoelectron ( $\mu$ ), its collection and multiplication on the first dynode (*scale* and *v*). We have omitted other parameters that take into account the resolution effects of readout system or correspond to the cascade multiplication of the secondary electrons as they are out of scope focus of our analysis. Given our requirements for single photoelectron signal sensitivity MAPMTs of our choice should be able to detect with high probability single photon that reaches photocathode. In order to achieve this goal MAPMT should have high quantum efficiency of the photocathode as well as high collection efficiency of produced photoelectron combined with substantial signal multiplication to achieve good resolution of SPE peak. These characteristics were studied in bulk for all 27520 channels (430x64) during the different light conditions and for different supplied HV values.

Fig. 13 shows the distribution of parameter  $\mu$  which correspond to the average number of the photoelectrons produced during the measurements. This parameters represents the convolution of the MAPMT photocathode quantum efficiency and laser setup light intensity. Both characteristics should not depend on HV supply values and it is demonstrated on this figure by comparison of  $\mu$  values extracted for the measurements at 1000 V and 1100 V. However one can change the parameter by varying the laser light intensity which is evident from the left

shift of  $\mu$  values for lower light intensity measurements.

The other two free parameters are plotted on Fig. 14. They correspond to the average number of second-stage electrons produced on the first dynode by photoelectron (see Fig. 14a and average signal amplitude for single photoelectron spectrum (see Fig. fig:scale). Both parameters characterize mainly the amplifying subsystem of MAPMT and therefore should depend on supplied HV. The measurements at 1000 V and 1100 V confirm that amplification is improved at higher values of applied high voltage. Traditionally the second parameter (gain) is often used to describe the amplification abilities of photomultipliers and often used in calibration and reconstruction procedures. And it was shown that the extracted gains do not depend on the light conditions with a high degree of accuracy.

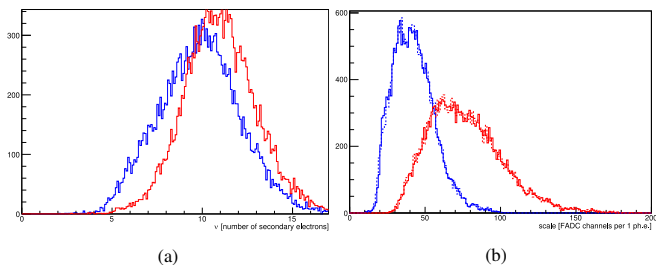


Figure 14: Characteristic parameters of single photoelectron signal distributions from Hamamatsu H12700 MAPMT in the framework of Pavel Degtiarenko's model for measurements at different HV: 1000 V (blue) and 1100 V (red): (a) average number of second-stage electrons knocked out of the first dynode, (b) the average signal amplitude per single photoelectron for different light intensity measurements: at  $10^{-5.4}$  (solid line) and at  $10^{-4.6}$  (dashed) attenuation

## 5. Maroc chip calibration

To remove the non-linearity within the ADC readout, a procedure was developed to convert the amplitude of the MAROC slow shaper signal from ADC channels into charge. The MAROC has a built-in charge injection functionality consisting of a test input pin which is connected to the preamplifiers through a logic network of switches and 2 pF capacitors. Together with an external step function generator, this can be used to inject a controllable amount of charge directly into the preamplifiers. We measured the output of the slow shaper in ADC channels for 82 different input charges ranging from 0 to 4 pC. Fig. 15 shows the relationship between the injected charge and the measured amplitude in units of ADC channels for three different readout channels. The relationship between charge and ADC channels is linear up to about 1.5 pC. This distribution was observed to vary between chips and pixels, and thus a unique distribution was measured for all 64 pixels on each MAROC used in this study.

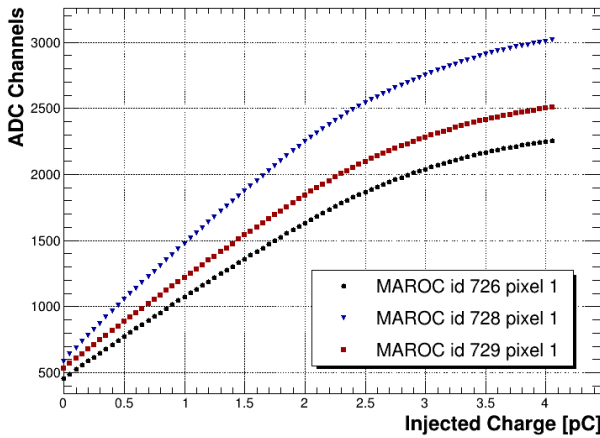


Figure 15: Response of MAROC slow shaper in ADC channels as a function of the injected charge. This curve is for MAROC id 726 and pixel 01.

This calibration data was used to convert the measured amplitude in ADC channels into charge collected on an event-by-event basis. The interpolation is done by assigning quadratic functions to every calibration data point to obtain local estimates of the charge as a function of ADC channels. The quadratic functions are obtained by fitting the nearest 5 data points, so that the value of the function is not constrained to equal the measured ADC channels at the given injected charge. For each event, the charge is estimated as a linearly weighted average between the extrapolations of the quadratic functions from the nearest two data points. Fig. 16 and Fig. 17 show typical amplitude distributions before and after this conversion is applied for one H12700 MAPMT pixel and one H8500 MAPMT pixel, respectively. For both, the conversion to charge extends the high-amplitude tails of the spectra due to the nonlinearity of the ADC readout.

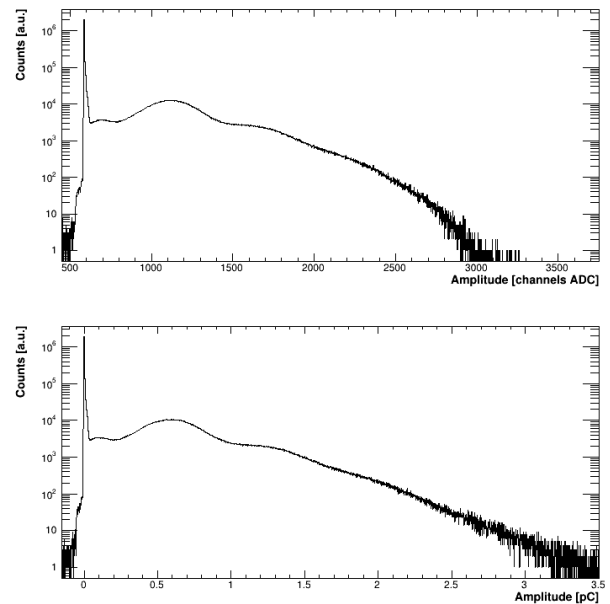


Figure 16: Top: A typical spe spectrum for one HA12700 pixel in units of ADC channels. Bottom: The same spectrum after converting the units into pC.

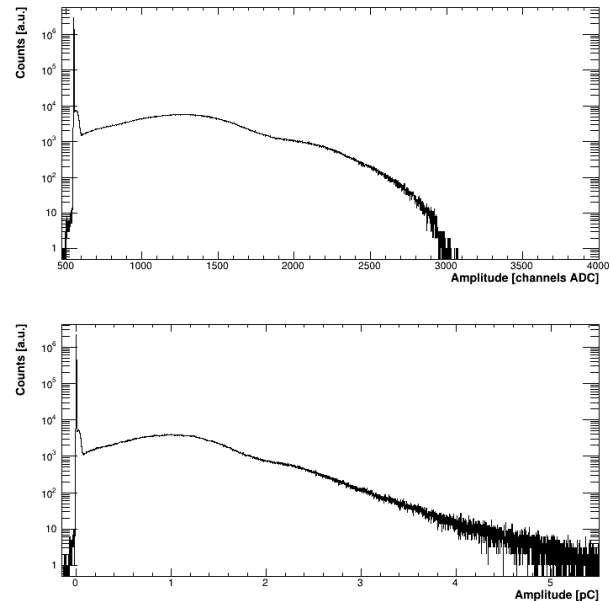


Figure 17: Top: A typical spe spectrum for one HA8500 pixel in units of ADC channels. Bottom: The same spectrum after converting the units into pC.

## 6. Cross talk measurements

Electronic crosstalk is present in both the H12700 and H8500 MAPMTs. This is best observed by plotting the measured charge in one pixel vs. the measured charge in an adjacent pixel. Fig. 18 and Fig. 19 show these two dimensional plots for all pixels which neighbor pixel 28 for one H12700 MAPMT and one H8500 MAPMT, respectively. The crosstalk bands are most prominently seen in the pixels directly to the left or right, where the amount of charge collected in one pixel is shown to be proportional to the charge measured in the adjacent one. In particular the bands with a high slope correspond to events where the the pixel plotted on the vertical axis measures some light and the pixel plotted on the horizontal axis has a small amount of charge resulting from electronic crosstalk.

Because the crosstalk events are easily characterized as sloped bands in these two dimensional plots, a simple method was developed to remove the crosstalk offline on an event-by-event basis. For each event the charge collected in a single pixel was compared to the maximum charge collected in the neighboring pixels. This cut is illustrated in Figs. 18 and 19 as the dashed (red) line drawn on each 2-dimensional plot. The start of the cut line is placed  $7\sigma$  above the pedestal to avoid removing events belonging to the pedestal distribution. Although the slope of the crosstalk bands can vary between pixels, the slope of the cut line used here is the same for each pixel. The main drawback of this crosstalk cut is that it removes events where adjacent pixels both happen to have a photoelectron emitted from the same laser trigger. However, the fraction of these accidental coincidence events is low when the laser filter is used at the minimal setting. The charge spectra before and after the removal of the crosstalk events in this manner is compared in the central plot in Figs. 18 and 19. For both the H12700 pmt and the H8500 the contribution of the crosstalk to the amplitude spectra appears as a shoulder to the pedestal distribution. However, the relative degree of the crosstalk amplitudes between the two different pmts is quite different. For the H12700 pmts, the crosstalk amplitude is roughly 2-3% of the amplitude from the pixel where light is incident. In contrast, for the H8500 pmts the ratio of the crosstalk amplitude to the signal amplitude can be as high as 50% in some pixels.

As a comparison for the offline crosstalk removal, we collected data where all pixels on the pmt were masked by a black sheet of paper. A 3mm diameter hole was punched over the center of a single pixel to measure the charge spectrum free from crosstalk from the neighboring pixels.

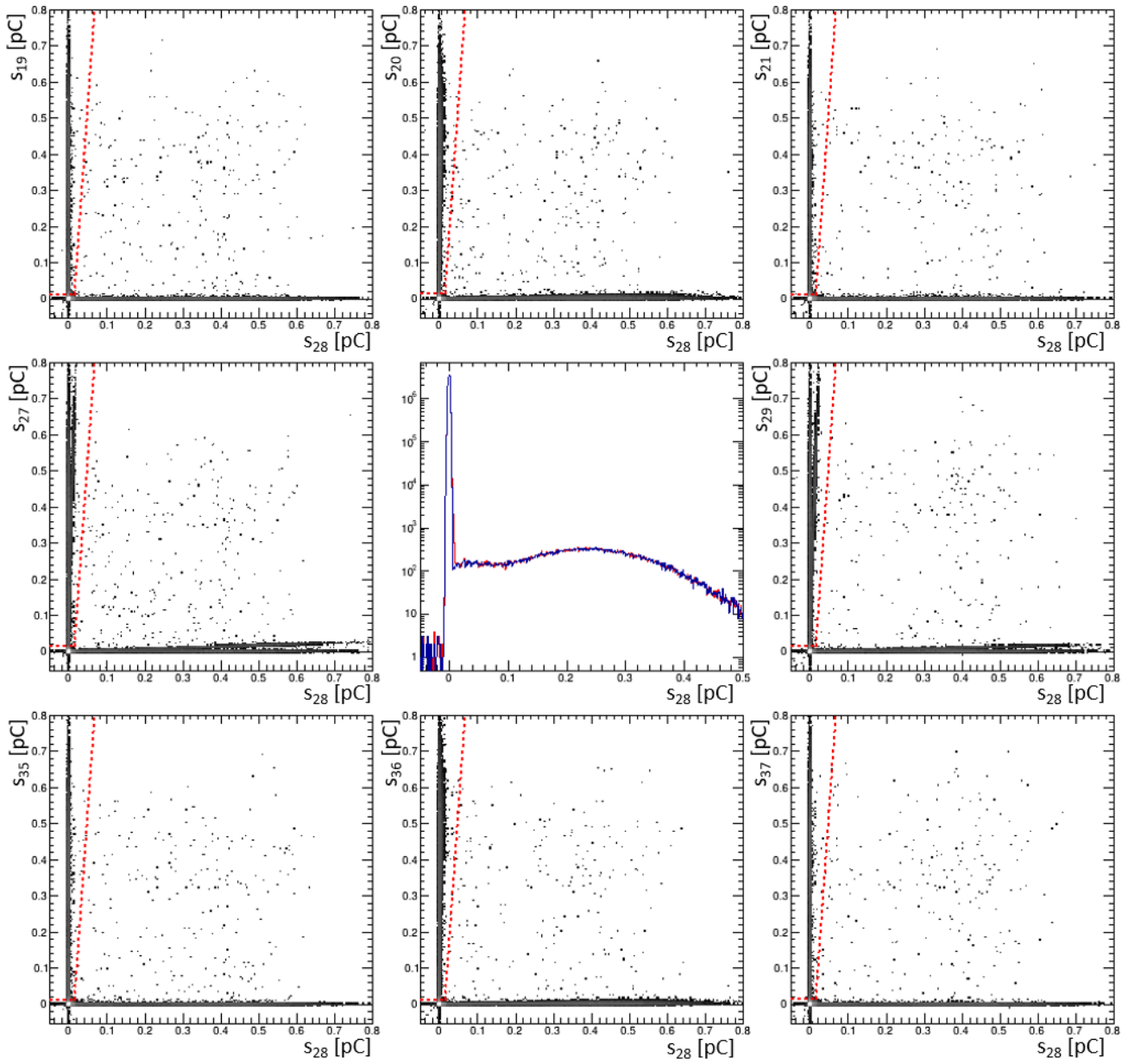


Figure 18: The charge measured in adjacent pixels is plotted as a function of the charge measured in pixel 28 for a typical H12700 MaPMT. The central plot shows the charge spectrum before (red) and after (blue) removal of the crosstalk events which are cut by the dashed (red) line on the 2-dimensional plots.

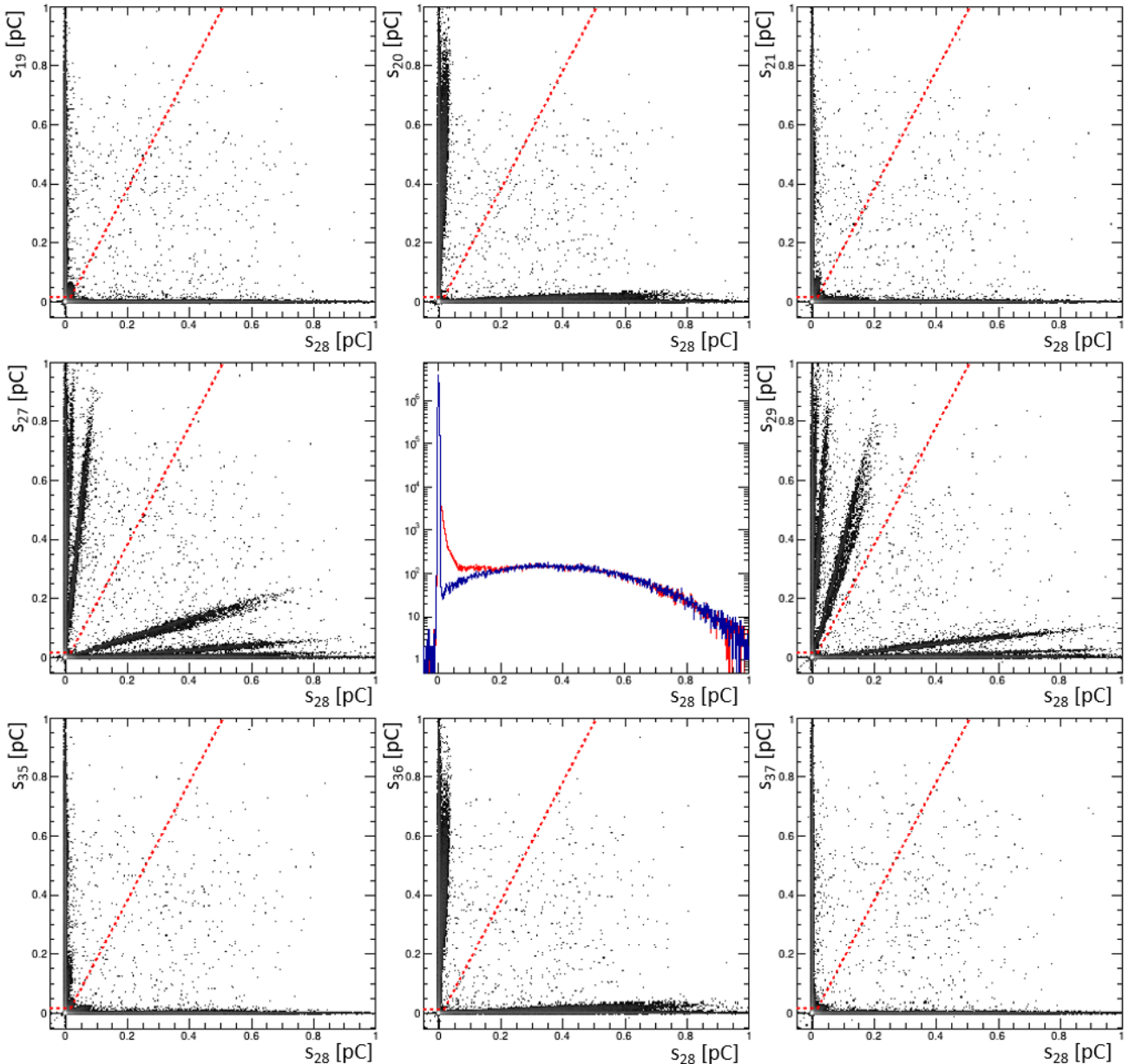


Figure 19: The charge measured in adjacent pixels is plotted as a function of the charge measured in pixel 28 for a typical H8500 MaPMT. The central plot shows the charge spectrum before (red) and after (blue) removal of the crosstalk events which are cut by the dashed (red) line on the 2-dimensional plots.

## 7. Results

We saw that although there is little difference in crosstalk signals, the H12700 PMTs suffer less from dark current, have narrower SPE spectra, and have higher  $\mu$  and relative efficiency values.

We see that the relative efficiency is closely related to the  $\mu$  which is on average, over all pixels at all voltages for all the PMTs we tested,  $29 \pm 5$  percent higher in H12700 than H8500 MAPMTs. One concern with these  $\mu$  measurements however is that the laser system used to measure these PMTs was only incident on a portion of each pixel, consequently missing their sum total effect and pinpointing possible spatial dependencies which should be further studied and perhaps remeasured with a fully illuminated MAPMT instead of collimated pinpoint laser light. In terms of crosstalk for the two varieties of MAPMT the H12700s appear to be better than the H8500s. The H12700s have a decrease in crosstalk by nearly a factor of two. Additional studies of dark current in the H12700s would be useful, as the dark current is usually dominated by individual pixels or bad regions of the PMT instead of spread around evenly like in the H8500s, but overall the two varieties are not very different in terms of dark current.

## **8. Conclusion**

## References

- [1] H. Avakian, et al. (CLAS), Measurement of Single and Double Spin Asymmetries in Deep Inelastic Pion Electroproduction with a Longitudinally Polarized Target, *Phys. Rev. Lett.* 105 (2010) 262002.
- [2] V. D. Burkert, et al., The CLAS12 Spectrometer at Jefferson Laboratory, *Nucl. Instrum. Meth.* A959 (2020) 163419.
- [3] M. Contalbrigo, et al., The CLAS12 Ring Imagine Cherenkov Detector, *Nucl. Instrum. Meth.* A960 (2020) 22–27.
- [4] M. Contalbrigo, et al., Single photon detection with the multi-anode CLAS12 RICH detector, *Nucl. Instrum. Meth.* A952 (2020) 162123.
- [5] M. Mirazita, et al., The large-area hybrid-optics RICH detector for the CLAS12 spectrometer, *Nucl. Instrum. Meth.* A876 (2017) 54–58.
- [6] M. Contalbrigo, et al., The large-area hybrid-optics CLAS12 RICH detector: Tests of innovative components, *Nucl. Instrum. Meth.* A766 (2014) 22–27.
- [7] Hamamatsu multianode pmt h8500, (????). [https://www.hamamatsu.com/resources/pdf/etd/H8500\\_H10966 TPMH1327E.pdf](https://www.hamamatsu.com/resources/pdf/etd/H8500_H10966 TPMH1327E.pdf).
- [8] Hamamatsu multianode pmt h12700, (????). [https://www.hamamatsu.com/resources/pdf/etd/H12700\\_H14220 TPMH1379E.pdf](https://www.hamamatsu.com/resources/pdf/etd/H12700_H14220 TPMH1379E.pdf).
- [9] E. H. Bellamy, G. Bellettini, F. Gervelli, M. Incagli, D. Lucchesi, C. Pagliarone, F. Zetti, Yu. Budagov, I. Chirikov-Zorin, S. Tokar, Absolute calibration and monitoring of a spectrometric channel using a photomultiplier, *Nucl. Instrum. Meth.* A339 (1994) 468–476.
- [10] P. Degtiarenko, Precision analysis of the photomultiplier response to ultra low signals, *Nuclear Instruments and Methods in Physics Research Section A: Accelerators, Spectrometers, Detectors and Associated Equipment* 872 (2017) 1 – 15.